Understanding the Hydration Process of Salts: The Relation between Surface Mobility and Metastability

Jelle Houben, Dennis Langelaan, Luc Brinkman, Henk Huinink,* Hartmut R. Fischer, and Olaf C.G. Adan

Read Online

ACCESS | Metrics & More | Article Recommendations

ABSTRACT: In this work, the relation between mobility and metastability is investigated. This is done under pure water vapor vacuum conditions. First, the properties of the metastable zone under pure water vapor conditions are investigated and compared to those under atmospheric conditions. Second, mobility is investigated using electrochemical impedance spectroscopy, whereby we differentiate between bulk and surface mobility. Using surface mobility, we showed that mobility is a prerequisite for the nucleation of K_2CO_3. Sufficient mobility must be introduced for the diffusion of ions and water, whereby an increase of almost two orders of magnitude (800 times) is observed on a hydrated sample. It has been shown that the metastable zone is both a consequence of the energy barrier for nucleation and the low ion mobility at low vapor pressures.
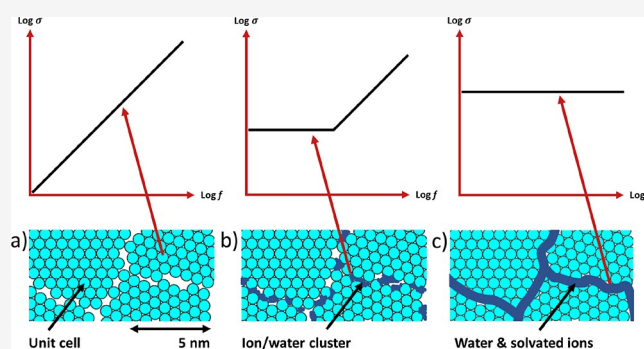
1. INTRODUCTION

Significant growth in the global population has put a heavy load on fossil fuels such as coal and oil, which are estimated to be exhausted in a couple of decades.[1] Moreover, these fossil fuels are leading to increased CO_2 emission, which is the major greenhouse gas (GHG) contributor and the cause of global warming.[2] To reduce the GHG emissions, a transition from fossil fuels to renewable energies has to be made. Solar energy is regarded as one of the most promising renewable energy source.[3] Solar energy, like other renewable energy sources, is characterized by its intermittent behavior, originating from the variations in solar irradiation with the weather, location, time, and season of the year.[4] Therefore advanced energy storage is a crucial technology for a widespread integration of renewable energies in our total energy supply.

Thermochemical energy storage is a promising candidate for advanced energy storage as it offers a high energy storage density (ESD, specific thermal storage capacity) and negligible heat loss.[5,6] Thermochemical heat storage is based on reversible sorption reactions, which are used to store energy. Sorption is defined as the fixation or capture of a gas (called sorbate) by a solid or liquid (called sorbent).[7]

Salt hydrates are a promising subclass of thermochemical storage materials as they have a high energy density and charge and discharge temperatures suitable for the built environment and use an inherently safe sorbate (water vapor, which is non-toxic and environmentally friendly).[8] From an extensive review of 563 hydrate reactions, potassium carbonate (K_2CO_3) has been selected as one of the most promising materials for domestic heat storage based on the temperature operating window, stability, price, and safety.[9]

Furthermore, it is recently demonstrated by Sögütoglu et al.[10] that for K_2CO_3, the near-equilibrium region involves a metastable zone (MSZ), which can be described by classical nucleation theory. This zone is indicated by the dashed lines above and below the equilibrium lines of K_2CO_3 in Figure 1. In the work of Sögütoglu et al.,[10] it is hypothesized that the hydration reaction is a transition that is mobilized by a wetting layer and where the mobility of this wetting layer increases with increasing supersaturation. At the metastable boundary (where noticeable hydration rates start), instantaneous nucleation is expected.

The existence of a wetting layer is supported by the fact that under ambient conditions, a thin film of water coats polar surfaces like salts.[11] In the literature, it is shown that for particles of NaCl in sub-deliquescence conditions (RH < 75%), there is a significant amount of water reversibly
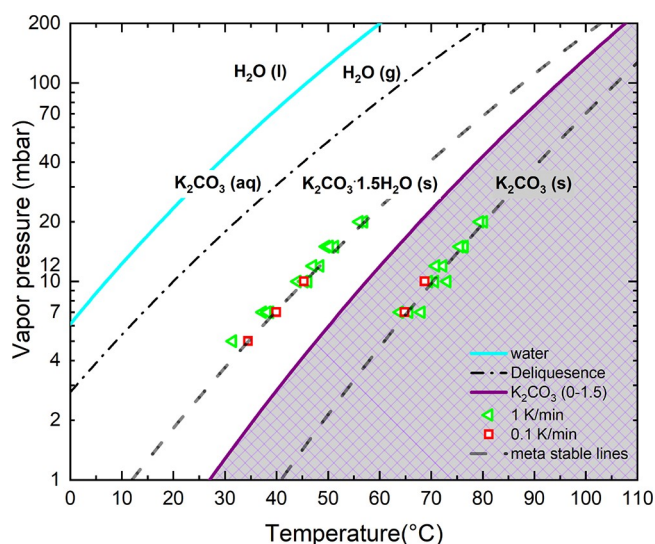
Figure 1. Blue triangles are the onset points found by Sögütoglu et al.[10] at a cooling/heating rate of 1 K/min and in atmospheric conditions, and red squares are the onset points at a rate of 0.1 K/min. The dashed lines are an extrapolation of these points.

associated with the surface of particles, where it is also hypothesized that an aqueous solution is present containing Na and Cl ions.[12] Other studies show that even far below deliquescence (RH = 40%), there is an adsorbed monolayer of water. This monolayer does not solvate the surface yet; however, between a relative humidity of 40 and 50%, there are the first signs of ion mobility.[13] Since to our knowledge no data is present in the literature about water adsorption and mobility on K_2CO_3, NaCl is used as a framework for the analysis of the relation between water adsorption, solvation, and mobility.

In this work, we explore the relationship between mobility and the metastable behavior of salt hydrates, K_2CO_3 specifically, which has a single hydration transition (0−1.5). We address the question if mobility is a prerequisite for the phase transition and which step in the phase transition is rate-limiting: ion mobility at the surface or nucleation of the new phase.

Since it is hypothesized that the phase transition is mediated by a local incipient dissolution of the ionic structure, it is expected that this mobility (local ionic solution) has a large effect on the electrical conductivity of a salt, especially since the bulk (salt crystal) is expected to have a low relative permittivity. As a consequence, the analytical measurement technique used should be very sensitive for low-conducting materials. Therefore, we used electrochemical impedance spectroscopy (EIS), enabling us to extract frequency-dependent information. This frequency-dependent conductivity (at various supersaturations) gives us more detailed information on the physical interpretation of the water adsorption mechanism.

Since in this work, the mobility is investigated under pure water vapor conditions and the metastable zone of K_2CO_3 was determined under atmospheric conditions (by Sögütoglu et al.[10]), the metastable zone first has to be verified under pure water vapor conditions. Furthermore, we have characterized the MSZ at higher temperatures and pressures. Finally, we want to prove the presence of the wetting layer and to investigate how this wetting layer is related to the hydration transition and its metastable behavior.

2. THEORY

In powdery systems and porous media with a high surface to volume ratio, surface properties play a major role in material behavior. The two most common surface properties that influence surface behavior are the surface charge and surface energy.[14] Close to the surface of NaCl ionic crystal, water dipoles are oriented normal to the surface mainly due to the electrostatic attraction between Na^+ ions and the oxygen atoms of water molecules.[15,16] The interaction of water with the surface may be enhanced by the presence of atoms that are able to form hydrogen bonds and charged sites.[17]

Since under ambient conditions, most surfaces are coated with a thin layer of water, it is important to understand how this water is being adsorbed. The retention or release of a liquid compound on a solid controls the mobility of many substances in the environment and has been described in terms of the "sorption isotherm".[18] For the adsorption of a monolayer, the simplest adsorption isotherm is given by Langmuir, which is based on dynamic stability. An equilibrium is established in which the rate of adsorption of molecules onto the surface equals the rate of desorption.[14]

In this work, we will not go into great detail on how water is exactly being adsorbed on specific sites of the ionic structure. Here, we are focusing initially on the stages of water adsorption in relation to the supersaturation and how this is connected to the metastable behavior and thus the nucleation of the hydrous (or anhydrous) phase. To get more insight into this nucleation behavior, we need to understand how the nucleation rate is affected.

The nucleation rate itself cannot be measured directly in the case of hydration. What can be measured though is the waiting period before the first nuclei are being observed. The latter is called the induction time from which the rate of nucleation can be determined[19] as it is inversely proportional to the induction period

$$\tau \propto \frac{1}{J} \tag{1}$$

where τ is the specific observable induction period. The nucleation rate is expressed in the form of an Arrhenius reaction rate equation:

$$J = \kappa \cdot \exp\left(\frac{-\Delta G^*}{k_b T}\right) \tag{2}$$

wherein J $[s^{-1}]$ is the nucleation rate, κ $[s^{-1}]$ a kinetic prefactor, G^* [J] is the nucleation free energy barrier, k_b [1.38 × 10^{-23} J/K] is the Boltzmann constant, and T [K] is the absolute temperature. The kinetic prefactor is not taken into consideration in the work of Sögütoglu et al.[10] but can play a critical role in the mechanism of salt hydrate phase transitions. The prefactor depends on the specific mechanism of cluster formation and is defined as[20]

$$\kappa = Z(\nu A^*)\rho_\nu \tag{3}$$

where νA^* $[s^{-1}]$ is the rate of addition of molecules to the critical cluster, ρ_ν $[kg/m^3]$ is the density of the supersaturated vapor, and Z [−] is the Zeldovich factor.[20]

If an assumption is made for the geometry of the cluster, e.g., two-dimensional, a critical energy barrier can be determined as

$$\Delta G_{2D}^* = \frac{h\pi\nu\gamma^2}{(b-a)k_bT\ln(p/p_{eq})} \tag{4}$$

where h [m] is the height of a discus shape cluster, ν [m^3] is the volume of one hydrated salt unit, γ [J/m^2] is the gas−liquid interfacial surface tension, a and b [−] are the number of water molecules in the beginning and end phase, respectively, and p/p_{eq} [−] is the supersaturation. For a three-dimensional geometry, the energy barrier can be determined as

$$\Delta G_{3D}^* = \frac{\eta\pi\nu^2\gamma^3}{(b-a)^2(k_bT)^2\ln^2(p/p_{eq})} \tag{5}$$

Here, η [−] is the shape factor of a 3D cluster, that is 16/3 if we assume a spherical geometry and 8/3 for half a sphere (hemisphere). For a full derivation and material parameters, we refer to Sögütoglu et al.[10]

The only unknowns in eqs 4 and 5 are the interfacial energy γ and J where J is inversely proportional to τ and can be determined experimentally at different supersaturations p/p_{eq}. When plotting the experimentally determined induction times against the corresponding supersaturations ($\ln(p/p_{eq})$ for 2D and $\ln^2(p/p_{eq})$ for 3D), the interfacial energies can be determined by the slope of data points.

The other unknown is the nature of the mechanism of cluster formation, which is described by the prefactor in eq 3, and this mechanism is the key topic of this work and will be investigated by probing the ion mobility as a function of supersaturation (in and outside the metastable zone) in order to link mobility to the hydration transition.

3. MATERIALS AND METHODS

3.1. Materials. For the two types of experiments, different setups are used resulting in different sample requirements. We have used K_2CO_3-based particles with a size of 1.4−2.0 mm and 50 g sample size. More details about the material can be found elsewhere.[21] The material is shown in Figure 2.
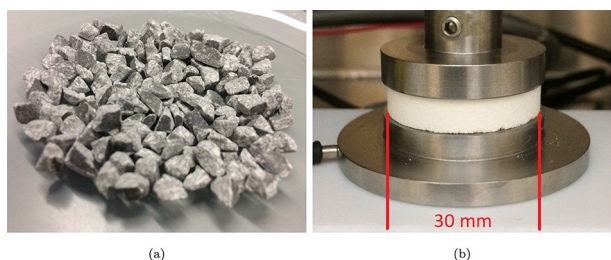

Figure 2. (a) Granules of compacted K_2CO_3 base material (97 wt %) and binder. (b) Pure K_2CO_3 tablet placed in between the electrodes.

For the conductivity measurement using electrochemical impedance spectroscopy (EIS), tablets are pressed as shown in Figure 3. The use of tablets instead of powder has two reasons; the sample must be placed in between two electrodes and the outside of the sample must be accessible for water vapor. The tablets are compressed from anhydrous K_2CO_3 (ACS grade) supplied by Sigma Aldrich and hydrous K_2CO_3 supplied by Alfa Aesar. The powder is sieved in a fraction of 150−300 μm to reduce effects caused by particle size variation. The compression is performed by a manual hydraulic press using a force of 1.1 kN. The anhydrous tablet is 30 mm in diameter, with 5.28 mm thickness and a mass of 5.96 g, with a porosity of 34%. The hydrous tablet is 30 mm in diameter, with a thickness of 5.17 mm and mass of 6.00 g. This results in a porosity of 32%.

3.2. Hydration Setup. For the determination of the MSZ and the induction times, a small-scale hydration setup is used. The setup consists of an evaporator/condenser and a TCM compartment, in which the temperature and vapor pressure can be controlled. The sample temperature and sample mass are measured so that the onset of hydration or dehydration can be determined. A comprehensive description of the setup can be found elsewhere.[21]

3.3. Metastable Zone Determination. The metastable zone boundaries are defined by measuring the onset points of hydration or dehydration. This is done by measuring the sample temperature at a fixed heating or cooling rate by which the hydration or dehydration points can be determined by a change in sample temperature. The metastable zone width (MZW) is determined by heating/cooling the sample at a fixed rate (0.9, 0.4, 0.09, and 0.04 K/min) in isobaric water vapor conditions in a pure water vapor atmosphere. The onset point is determined by the point where the sample temperature starts to deviate from the imposed temperature due to the heat released by the hydration reaction (for more details, see our previous study[21]).

3.4. Induction Time Measurement. Before each induction measurement, the sample is prepared as a full hydrate or anhydrate. This is done in situ in isothermal and isobaric conditions. The induction time experiments are performed in isothermal and isobaric conditions as well.

At the start of each experiment, the sample is thermally equilibrated and subsequently water vapor is supplied. The induction period is then established as the period between the supply of water vapor and the onset of hydration. The onset of hydration is determined by the sample temperature as the sample temperature measurement is more sensitive than the mass signal.

3.5. Electrochemical Impedance Spectroscopy. An in-house setup is developed to measure the impedance under controlled sample temperature and water vapor pressure. The conductivity is measured using an impedance analyzer, and the sample is placed in a pure water vapor environment, such that the water vapor transport is extremely fast. A schematic overview of the setup is shown in Figure 3.

To obtain a vacuum controlled environment, the sample is placed in a Binder VD 23 vacuum oven. All electrical components of the oven are decoupled from the inner chamber; therefore, no noise is introduced for the impedance measurement. Moreover, the inner chamber acts as a faraday cage for external noise. The temperature can be set from 15 °C above ambient temperature to 200 °C. The vacuum oven is connected via a flexible metal KF flanged vacuum hose to a water vessel. This vessel acts as an evaporator/condenser and is submerged in a thermostatic bath that is temperature-controlled between 1 and 80 °C with an accuracy of 0.1 °C (LAUDA RE 415 silver). The vapor pressure in the oven is measured using a Pfeiffer CMR 361 active capacitance transmitter with an accuracy of 0.2% of the measured value. Vacuum is applied using an Edwards RV8. The supply of vacuum and/or water vapor is controlled using Pfeiffer solenoid actuated mini-angle valves. The sample temperature is measured using a type K thermocouple, and data acquisition is done with a National instruments NI 9211 thermocouple input module. The thermocouples are inserted via a vacuum feed-through connected to the DN 16 access port of the oven.

The electrodes of the potentiostat are also inserted via a BNC vacuum feed-through connected to the same port in the oven. The electrodes are made out of stainless steel, with a thickness of 5 and a diameter of 32 mm for the upper electrode. The lower electrode consists of two cylindrical parts, the part in contact with the tablet is 32 mm and the lower part is 5 mm, both with a thickness of 5 mm. The potentiostat is an Ametek Versastat 4. Measurements are performed in potentiostatic mode with an AC voltage amplitude of 1000 mV and frequency range from 0.1 Hz−1 MHz. The current is measured using a low current interface (LCI), by which a minimum current of 4 pA can be measured with a resolution of 122 aA.

4. RESULTS

4.1. Metastable Behavior. Since in this work, the mobility is investigated under pure water vapor conditions and the
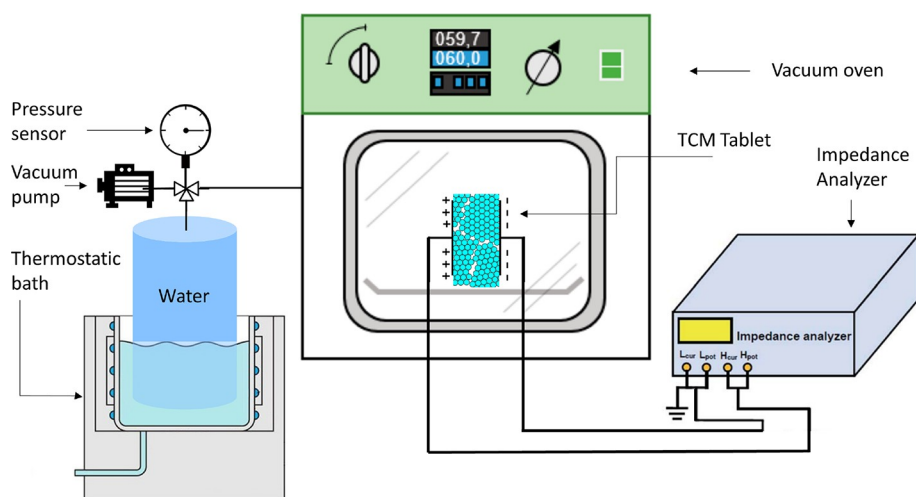
Figure 3. Schematic representation of the measurement setup. Center: the vacuum oven in which the sample is positioned; left: the thermostatic bath which supplies the water vapor; right: the impedance analyzer.

metastable zone of K_2CO_3 was determined under atmospheric conditions (by Sögütoglu et al.[10]), the metastable zone first has to be verified under pure water vapor conditions.

This is done using the reactor setup (3.2). The results are plotted in a phase diagram; herein, the partial water vapor pressure p is plotted as a function of temperature T of the salt. The equilibrium hydration line has been determined in a previous study by measuring equilibrium pressure−temperature points under pure water vapor conditions.[21] The phase diagrams with the onset points of hydration and dehydration are shown in Figure 4. The metastable zone under these pure water vapor conditions is then compared to the metastable zone under atmospheric conditions as found by Sögütoglu et al.[10]

The solid line represents the equilibrium line of K_2CO_3; above this line, the 1.5 hydrate is the thermodynamically favored phase and below, it is the anhydrate. The dashed lines are the MSZ boundaries as measured in atmospheric

conditions.[10] The closed symbols are the hydration/dehydration onset point at different cooling/heating rates as measured by the pT-mass setup. The open circles will be discussed in Section 4.3.2.

Under pure water vapor conditions, the onset points for both hydration and dehydration match very nicely with the onset points in atmospheric conditions. Moreover, since in this setup, it is possible to measure over a broader range of temperatures and vapor pressures, the metastable zone is measured at higher temperatures and pressures, showing that the extrapolation (dashed lines) of Sögütoglu et al.[10] holds also for higher temperatures and pressures.

Under atmospheric conditions, no dependency was found for the onset points at different cooling/heating rates (0.1, 0.5, and 1 K/min). Under pure water vapor conditions, the cooling rate dependency of the onset points is shown in Figure 4.

The blue squares are the hydration/dehydration onset points at a rate of 0.9 K/min. These points match nicely with the metastable line under atmospheric conditions (dashed lines). The green circles, blue squares, and oranges stars are the onset points at rates of 0.4, 0.09, and 0.04 K/min, respectively. It can be seen that by lowering the cooling rate, the hydration onset line shifts toward the equilibrium line. This is at least not significantly observed by Sögütoglu et al.[10] under atmospheric conditions, see Figure 1. A shift in onset points toward equilibrium indicates that the induction time for hydration/dehydration is lowered. The induction time is inversely proportional to the nucleation rate. Referring to eq 2, where the nucleation energy barrier does not change by changing the cooling/heating rates in the latter experiment, the change in nucleation rate J can only be caused by a change in the kinetic prefactor. This suggests that the thermodynamic prefactor is influenced by the transport mechanism of water vapor. Note that the measurements by Sögütoglu et al.[10] are performed at lower temperatures. At these temperatures, no large influence of the heating/cooling rate is observed.

4.2. Nucleation. To get more insight in the nucleation process, induction time measurements are performed. Since induction times are inversely proportional to the nucleation rate (see eq 2), these types of experiments give insights into the nucleation barrier.
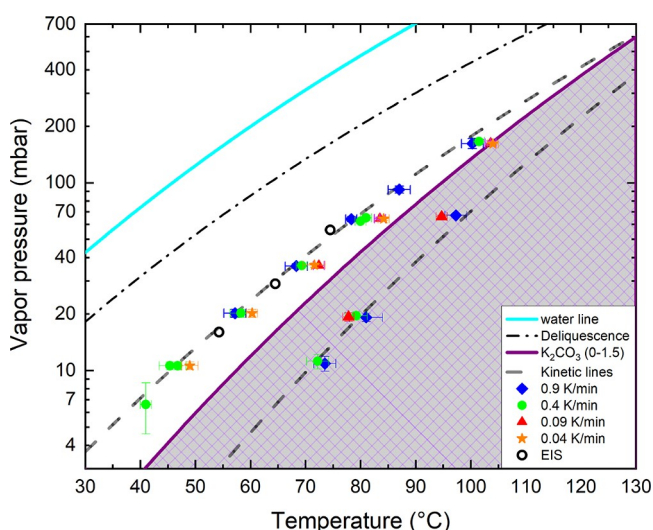

Figure 4. Different markers indicate onset points found in pure water vapor conditions at different heating/cooling rates as indicated in the legend. The dashed line is an extrapolation of the onset points found under atmospheric conditions by Sögütoglu et al.[10] at a cooling/heating rate of 1 K/min.
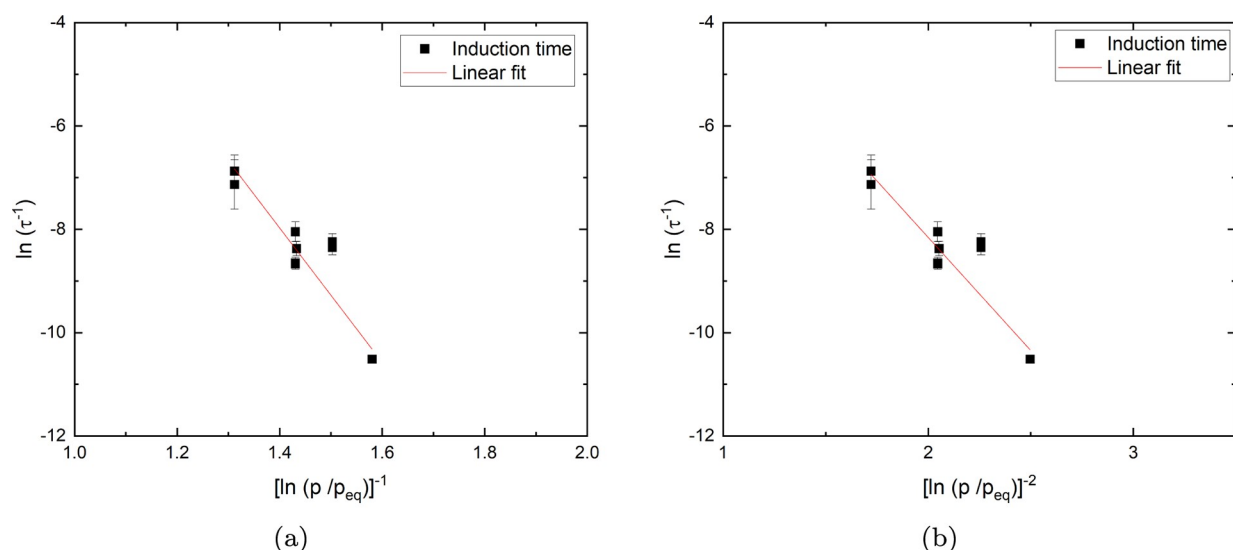
Figure 5. (a) Linear fit for a 2D geometry; induction times as a function of the inverse of the supersaturation (p/p_{eq}) at a sample temperature of 54 °C. (b) Fit for a 3D geometry; induction times as a function of the inverse of the supersaturation squared.
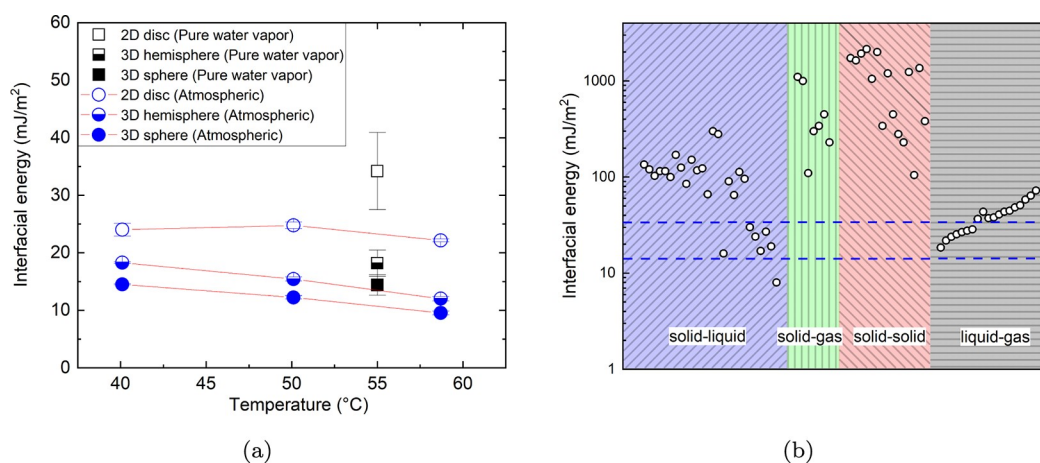

Figure 6. (a) Interfacial energies calculated for various critical cluster shapes in pure water vapor conditions compared to atmospheric conditions of Sögütoglu et al.[10] (b) Derived interfacial energies compared to interfaces for various interfaces.[22−26] The dashed lines indicate the range of values found for pure water vapor conditions.

The induction times are measured at a temperature of 54 °C and at various supersaturations (p/p_{eq}). The interfacial energies γ can now be obtained by fitting the induction time against supersaturation according to a 2D disc and 3D sphere or hemisphere nucleation model from eqs 4 and 5. Rewriting eq 2

$$\ln(\tau^{-1}) = \ln(\kappa) - \lambda \frac{1}{[\ln(p/p_{eq})]^n} \tag{6}$$

with $n = 1$ and 2 for 2D and 3D geometry, respectively, using eqs 4 and 5, λ [−] contains the interfacial surface energy γ and relates to the energy barrier for nucleation:

$$\lambda_{2D} = \frac{h\pi\nu\gamma^2}{(kT)^2(b-a)} \tag{7}$$

$$\lambda_{3D} = \frac{\eta\pi\nu^2\gamma^3}{(kT)^3(b-a)^2} \tag{8}$$

The results are shown in Figure 5a and show the linear fit according to eq 8.

Since the setup is not able to measure mass deviation accurately at timescales below 10 min, induction times at supersaturations above 2.2 are too short to be observed. This is due to mechanical equilibration after switching the valve at the water vapor pressure inlet. Moreover, at a supersaturation below 1.8, the experimental times would be too long.

The obtained interfacial free energies are shown in Figure 6a, where in Figure 6b, these energies are compared to interfacial solid−liquid, solid−gas, solid−solid, and liquid−gas interfaces.

The interfacial energies in pure water vapor conditions are in the range of 14−34 mJ/m². This is in range with values found under atmospheric conditions. Comparing the interfacial energy of 14−34 mJ/m² to literature values for different types of interfaces, see Figure 6b, shows that the solid−gas and solid−solid interfacial energies are significantly higher. Therefore, this indicates that in pure water vapor conditions, the interface at the nucleation site is covered by a liquid interface, which is in agreement with the work of Sögütoglu et al.[10] Note that comparable interfacial energies were found for other salt
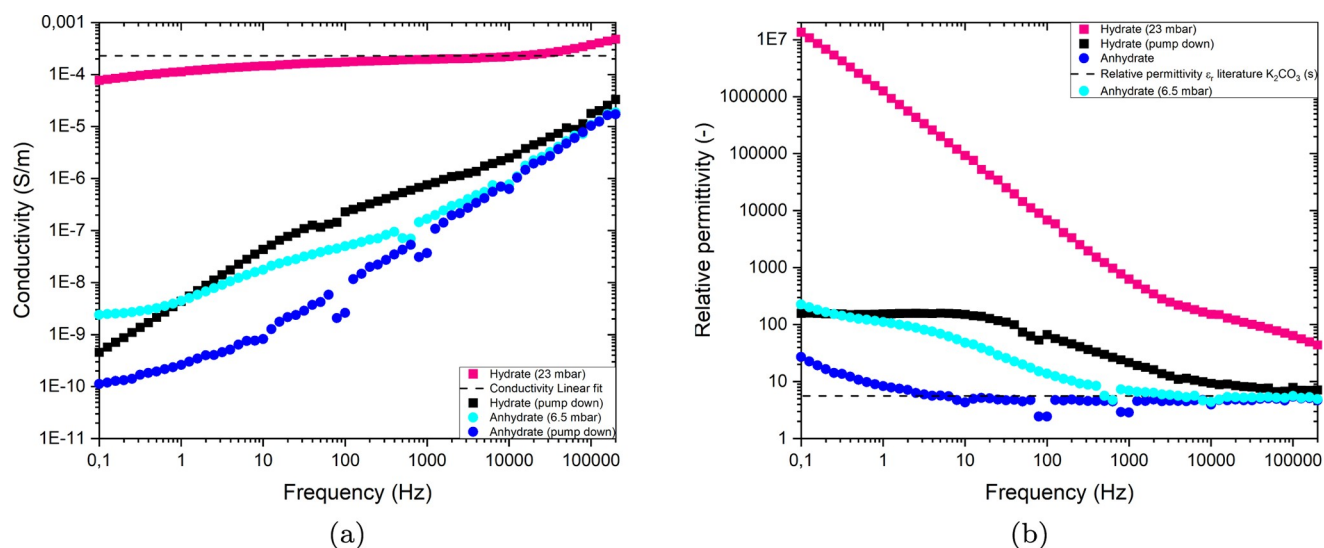
Figure 7. (a) Measured conductivity of both anhydrous (light and dark blue dots) and hydrous (pink and black squares) K_2CO_3 tablets at 54 °C in both the presence and absence of water vapor. (b) Related relative permittivities of both tablets. The horizontal dashed line is the permittivity found in the literature for K_2CO_3.[27]

crystal−solution interfaces of soluble salts, e.g., $Na_2S_2O_3\cdot 5H_2O$, KCl, KBr, KI, NH_4Br, and NH_4I.[22]

4.3. Surface Mobility. Now that the metastable zone under pure water vapor conditions corresponds to the metastable zone under atmospheric conditions, we investigate the relation between ionic conductivity and metastability. The ionic mobility is investigated with EIS both in and outside the metastable zone. First, it is investigated if it is possible to differentiate between surface and bulk conductivity. After that, we focus on the relation between water adsorption, mobility, and supersaturation (p/p_{eq}). In the final section, we will go into more detail on the structure of mobile ion−water clusters at the salt surface.

4.3.1. Probing Surface or Bulk Conductivity. In this section, we investigate if the measured ionic mobility can be attributed to the ion motion at the surface. Four cases have been studied: both an anhydrous and a hydrous tablet in the presence and absence of water vapor. All measurements are performed at 54 °C.

First, we will have a look at the anhydrous phase (see Figure 7 (dark blue dots)). Figure 7 shows the conductivity and relative permittivity as a function of frequency. The sample is prepared as a completely anhydrous tablet, and no water vapor is supplied during the measurement (continuous pump down of the system).

At every decade in frequency, there is a small disturbance in the data, most notably at low conductivity. This is caused by the impedance analyzer as its hardware (analog filters) switches internally at these points. The anhydrate in the absence of water vapor shows that the conductivity increases as a function of frequency and behaves like a power law. This indicates that the behavior is predominated by its capacitive character and only polarization occurs in the samples. A measure of polarizability is the permittivity of a material, where a constant permittivity indicates that no conductive behavior is present in the sample. This is shown in Figure 7b. Above 10 Hz, the data are fitted (not shown here), resulting in a permittivity of 4.5 [−]. This permittivity matches well with the permittivity of 5.6 [−] reported in the literature for K_2CO_3.[27]

Below 10 Hz, some mobility is still observed, which is probably due to some water still being present on the surface.

Second, we looked at the case of supplied water vapor at 6.5 mbar to the anhydrous sample (light blue). At 54 °C, the equilibrium pressure is 8 mbar; therefore, 6.5 mbar is just below equilibrium ($p/p_{eq} < 1$) and there will be no hydration reaction (see Figure 1). Consequently, we are only looking at adsorbed water at the surface and not at the hydration reaction. It can be seen that conductivity changes significantly in the presence of water at a low frequency. At 0.1 Hz, the conductivity increases with more than one order of magnitude compared to the vacuum case. This demonstrates that conductivity in the anhydrous phase is present due to water-assisted ionic mobility at the surface of crystals.

Third, the hydrate is prepared and is measured at a water vapor pressure of 23 mbar (pink squares), which is outside the metastable zone (see Figure 1). Figure 7a shows that in the presence of water, the conductivity as a function of frequency is almost constant over the entire frequency domain. The dashed line indicates a fit and results in a value of 1.9×10^{-4} S/m. This behavior completely differs from the anhydrous state, and this frequency independency indicates that the behavior is completely dominated by conduction.

In the hydrate at $p = 23$ mbar, significant mobility is observed. This may be caused by ionic mobility in the bulk of the salt or by surface water on the boundaries of the crystallites.

Fourth, to investigate the conduction mechanism, the hydrate is subjected to a continuous vacuum pump down. In this experiment, the conductivity is measured ($t \approx 10$ s) after pump down of the sample. Figure 7a (in the black squares) shows that the conductivity drops dramatically compared to that of the hydrous sample in a water vapor environment. Moreover, at higher frequencies, a plateau in permittivity is reached (Figure 7b), indicating that polarization is dominating and the conductive behavior has vanished. When water vapor is removed by a pump down, the behavior changes instantly from being conductive to being capacitive. This immediate response indicates that the water present (with dissolved ions) is quickly desorbed and that consequently the measured
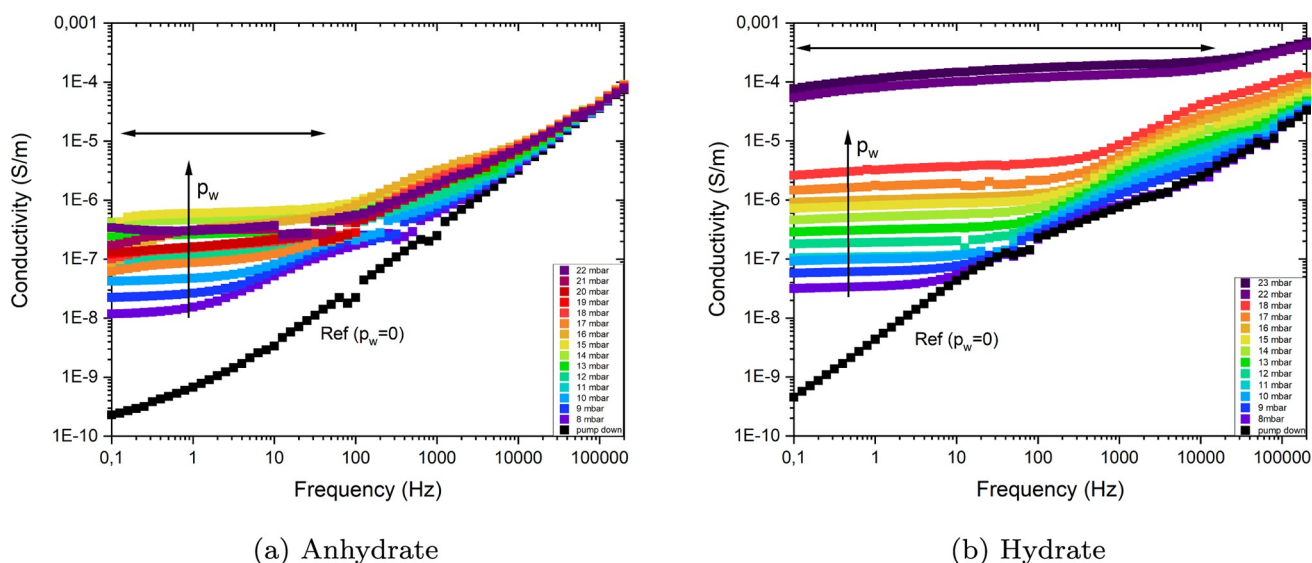
(a) Anhydrate

(b) Hydrate

Figure 8. (a) Conductivity measured in and outside the MSZ at 54 °C.

conductivity can only be attributed to ionic mobility mediated by water. This surface water mobilizes ions.

4.3.2. Metastability and Ion Mobility. In the previous sections, it was observed that the two extreme situations (hydrous versus anhydrous) had a clear distinction in the charge transport mechanism (conductive versus capacitive, respectively). Moreover, in the hydrous state, the response to changing water vapor conditions was extremely fast and pronounced, indicating that mobile water is present. Both measurements were performed outside the MSZ.

In this section, the mobility is addressed in the MSZ. We investigate if metastability might be linked to ion mobility facilitated by water adsorbed on the surface. In the metastable zone, there might be a lack of mobility and outside the MSZ sufficient, ion mobility may initiate bulk hydration. We focus on the kinetic prefactor of the nucleation rate.

First, we discuss the surface response of the hydrate $K_2CO_3 \cdot 1.5H_2O$. Second, we will investigate the surface mobility of the anhydrate K_2CO_3 as a function of the vapor pressure.

The measurements are done at a sample temperature of 54 °C and performed by increasing the water vapor pressure stepwise from 6 to 23 mbar, implying that we go from equilibrium through the MSZ toward outside the MSZ.

The vapor pressure dependencies of the anhydrate and hydrate are shown in Figure 8a,b, respectively.

In Figure 8a, the previously discussed anhydrate in the absence of water vapor (black markers) from Section 4.3.1 is plotted as a reference. Then, in purple, the conductivity is plotted at 8 mbar, which is just above the hydration–dehydration equilibrium. At this vapor pressure in the metastable zone, conductive behavior is already observed at frequencies below 10 Hz. This points at a low value for the surface conductivity. The number of mobile ions and their mobility are low at this water vapor pressure. This might indicate that the amount of adsorbed water molecules is too small to hydrate K_2CO_3, indicating that the hydration might be hampered.

Above 10 Hz, capacitive behavior, i.e., polarization of the crystal, is dominating. Increasing the vapor pressure from 8 to 23 mbar shows that the conductivity increases. Moreover, the frequency-independent (conductive) behavior is extended over

a broader frequency range, indicating that more ions can migrate faster over longer distances. Furthermore, it can be seen that above 18 mbar, the conductivity dramatically increases with the water vapor pressure; here also, some fluctuations can be observed, and this will be elaborated in Section 4.3.3.

Figure 8b shows the conductivity of the hydrate. At all vapor pressures, the conductivity is much higher for the hydrate than for the anhydrate sample. This is most pronounced at the highest vapor pressures of 22 and 23 mbar, which are outside the metastable zone. To analyze this in greater detail, the low frequency conductivity (0.1 Hz) is plotted as a function of the water vapor pressure in Figure 9, for two different temperatures, i.e., 47 and 54 °C.

Figure 9 shows that the conductivity and thus mobility increase significantly when the vapor pressure exceeds the MSZ boundary (vertical dashed lines). To confirm the correlation between the increase in mobility and the MSZ
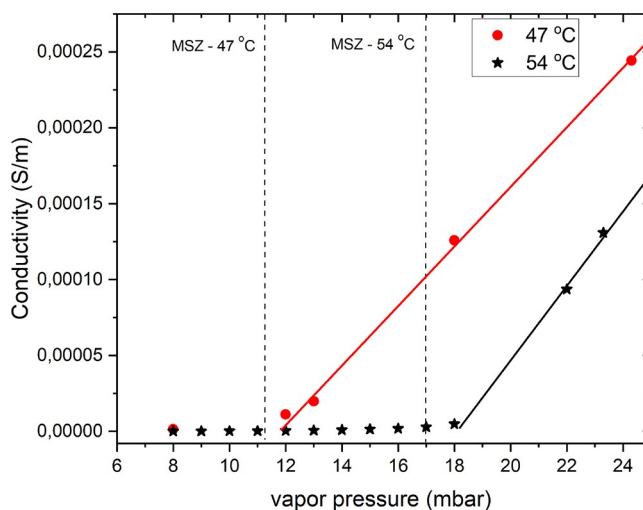

Figure 9. Conductivity at 0.1 Hz for a hydrate sample at 47 and 54 °C. As a guide for the eyes, the red and black lines are drawn to indicate the conductivity transition after the MSZ. The dashed lines indicate the metastable onset point for hydration as shown in Figure 1

boundary, the measurement series are also performed at a sample temperature of 47 °C. Again, a steep increase in conductivity is found when the pressure exceeds the MSZ boundary.

A significant shift in the slope of conductivity (at 0.1 Hz) as a function of water vapor pressure is observed in and outside the MSZ. Therefore, the mobility substantially increases while crossing the MSZ boundary.

The change in conductivity in and outside the MSZ is compared to that of the anhydrous sample. The results are shown in Figure 10.
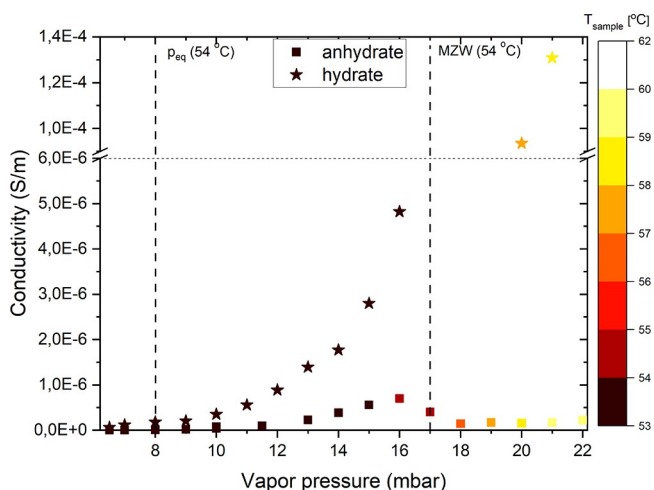

Figure 10. Conductivity at 0.1 Hz as a function of water vapor pressure for an anhydrate (squares) and hydrate (stars). The sample temperature is indicated by the color scale on the right.

The stars and squares indicate the conductivities of the hydrate and the anhydrate, respectively. Note that the conductivity on the y axis is now plotted on a linear scale and that there is a break in between 6.0×10^{-4} and 1.4×10^{-4} S/m, indicating the significant increase for the hydrate outside the MSZ. In the MSZ, there is ionic mobility both for the anhydrous (squares) and hydrous (stars) samples. However,

the mobility at the hydrate surface is much higher and increases more rapidly when approaching the MSZ boundary. Outside the metastable zone, the increase is steep. In the case of the anhydrous sample, the mobility drops at the MSZ boundary ($p > 17$ mbar). This is, presumably, due to the start of the hydration reaction at the MSZ boundary.

The start of the hydration actually starts at this point and is actually underlined in the measured sample temperature, which is indicated by the color scale on the right side of Figure 10. At vapor pressures below 17 mbar, there is no increase in the temperature of the sample. Above 17 mbar (vertical dashed line), the sample temperature increases significantly for both the hydrate and anhydrate. In the case of the anhydrate, this increase is caused by the exothermic reaction due to water absorption in the crystal (hydration reaction). In the anhydrate, this causes a drop in the conductivity, which is not the case for the hydrate.

More interestingly, in the hydrous sample, whereas no bulk hydration can occur as the sample is hydrated, an increase in mobility still shows. This increase may be caused by a change in water absorption or a change in salt dissolution.

To verify that this also holds over a broader range of temperatures and pressures, the experiment is repeated at a temperature of 64 and 74 °C. The onset points are shown in Figure 4 (open circles) and are determined by the change in mobility similar to the observation in Figure 10 at a temperature of 54 °C.

4.3.3. Structure of the Mobile Surface Layer. The previous sections show that mobility at the surface is due to the presence of water (with dissolved ions). How water and ions are present is however not yet clear. The frequency dependency of the conductivity and permittivity may give more information about the structure of water−ion clusters at the crystal surface and their mobility. In Figure 11, frequency dependencies of the conductivities and permittivities of an initial anhydrate phase at different water vapor pressures are shown.

First, we take a look at the drop in conductivity at the moment the MSZ boundary is crossed, above 28 mbar (indicated by the arrows). This drop corresponds to what was
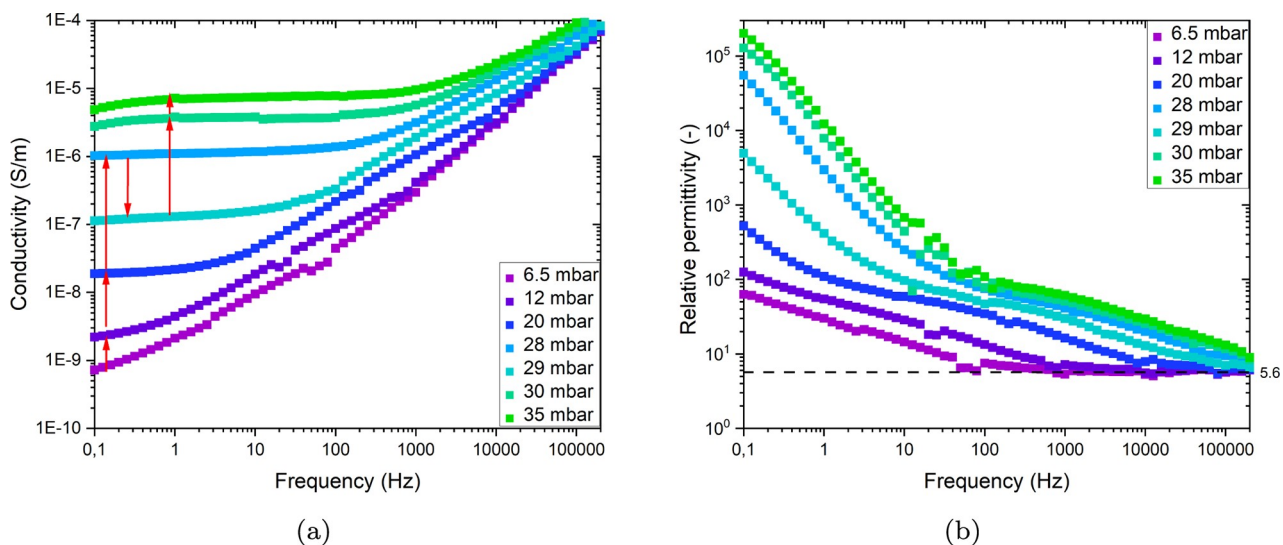

(a)

(b)

Figure 11. (a) Conductivity and permittivity of an initial anhydrate phase at different water vapor pressures at a sample temperature of 64 °C. The horizontal dashed line is the permittivity for the anhydrate as found in the literature.[27]

observed at 54 °C in Figure 10. Here, it can be seen that it occurs over the whole range of frequencies.

At low vapor pressures (6.5 and 12 mbar), the conductivity increases with increasing frequency over the whole frequency domain, indicating that polarization (of the induced dipoles in K_2CO_3) dominates. This is even clearer if we take a look at the permittivity in Figure 11b. Above 100 and 1000 Hz, the permittivity is constant and matches very well with the permittivity of 5.6 [−] for anhydrous K_2CO_3 as reported in the literature.[27] Below the 100−1000 Hz, the permittivity is no longer constant, indicating that there is not only polarization of the bulk crystal. However, the ionic mobility seems to be very localized as no long-range conduction is observed, i.e., no plateau in the conductivity. Due to the local character of the mobility, there must be a local cluster of dissolved ions wherein dissolved ions can move freely within the cluster boundaries. At the boundary, the charges become static until the polarity is reversed. Thus, within one period, between the switching of polarity, both conductive behavior (charge transport) and capacitive behavior (charge polarization) occur.

When the water vapor pressure is increased to 20 and 28 mbar (the system is still in the MSZ) in Figure 11b, the permittivity at high frequencies (>10 kHz) still equals 5.6 [−] as for a dry bulk crystal. This indicates that the mobility of the ions is not sufficient to follow the electrical field anymore. The onset points of local mobility shift, however, toward higher frequencies compared to those at 6 and 12 mbar. This indicates that more mobility is introduced at higher vapor pressures. Furthermore, looking at Figure 11a, the conductivity significantly increases (logarithmic y axis) and the conductive behavior dominates at lower frequencies (<10 Hz) as no frequency dependency is observed anymore. Due to water adsorption, the surface has become more mobile and charges can now be transported over longer distances. This indicates that the initial water clusters have grown in size and that small clusters have agglomerated into larger ones, which then facilitate charge transport over longer distances (conductive behavior). This results in the plateaus in Figure 11a. In Figure 11b, this can be observed in the second change in slope around 1 and 10 Hz at water vapor pressures of 20 and 28 mbar, respectively. Here, the permittivity is increasing significantly with decreasing water vapor pressure, indicating that the polarizability of the crystal is playing less of a role.

At 30−35 mbar, conductive behavior dominates up till 100−1000 Hz, considering the observed plateaus. The height of this plateau, i.e., the conductivity, increases. Figure 11b shows over the whole frequency range a changing polarization. This is similar to the observations at 28 mbar (in the metastable zone, close to the boundary).

5. DISCUSSION

Section 4.3.2 shows a link between ion mobility and metastability. Section 4.1 and Sögütoglu et al.[10] showed that the MSZ boundary can be linked with the existence of a nucleation barrier. It follows from classical nucleation theory (CNT) that the nucleation rate depends on two factors: the free energy barrier and cluster mobility. The latter is accounted for by the prefactor in the nucleation rate in eqs 2 and 3. Our findings on ion mobility point to the kinetic prefactor.

The kinetic prefactor depends on the specific dynamics of cluster formation. This factor was not taken into account in the previous work of Sögütoglu et al.,[10] which focused primarily on the nucleation barrier. It was shown that the induction times in

the MSZ could be characterized by CNT, whereby nucleation and growth are limiting the hydration rate in the MSZ.

The prefactor depends on the specific mechanism of cluster formation. Two distinct possibilities are discussed in the literature: (1) direct deposition of water vapor on the surface of the cluster and (2) surface diffusion of ions and water toward the nucleus and their attachment to it, at which surface mobility is needed.[20]

This work shows that onset points determined by the mobility nicely correspond to the MSZ boundary. Considering that a change in mobility corresponds to the onset of hydration (see Figure 10) implies that surface mobility strongly increases at the boundary of the metastable zone. It has been argued that mobility is needed in the case of cluster formation development via diffusion of ions and water toward the nucleus. Accordingly, mobility is limited in the metastable zone compared to that outside the MSZ. Therefore, diffusion of ions and water is limited too. To understand this sudden change in mobility at the MSZ boundary, we look at the solvation of ions and thereby focus on the solid−liquid interface. As discussed elsewhere,[13] for NaCl, a monolayer adsorption of water occurs at an RH of 40%. Thereafter, ion migration occurs at an RH between 40 and 50%. This is well below an RH of 75%, where dissolution of the bulk occurs (deliquescence), indicating that the solvation of NaCl requires a higher relative humidity than needed for water adsorption. This suggests that water molecules are taken up by the surface, but the solvation of the salt surface only starts when sufficient water molecules are present, facilitating the process. In AFM experiments of Xu et al.,[28] these structural effects are also found. They observed that the adsorbed water film hydrates NaCl ions, which become mobile on the surface.

Since there is a difference in energy required to solvate ions from smooth faces and from defect-rich crystallite surfaces,[13,29,30] the solvation in the MSZ will commence at defects and after this an induction period is required for these nuclei to stabilize and grow. Dai et al.[31] indeed reported that adsorbed water on a NaCl crystal surface probably solvates and detaches ions at the steps and this is then linked to differences in local water concentration, ionic solvation, and mobility. At low RH, water is primarily adsorbed on edges where there is a higher surface energy. Subsequently at medium humidity, step diffusion of the solvated ions takes place. This matches with our observation on K_2CO_3 that mobility is introduced even at low vapor pressures in the metastable zone. In this case, the frequency-dependent conductivity indicated that there must be localized mobility and thus clusters of water and ions. In the work of Foster et al.,[29] where the adsorption of water on NaCl has been studied, it is also reported that at low adlayer coverage, the water molecules aggregate into islands. Moreover, they report that when a critical adlayer concentration is reached, multilayer growth suddenly becomes favorable. This matches with our observation that the mobility increases dramatically above the MSZ and that there is a link between mobility and metastability. Finally, it is stated that as adlayer coverage increases, solvation starts and new adlayer structures can develop. This matches very well with our water absorption mechanism analysis of K_2CO_3 based on mobility, i.e., water adsorption, cluster formation, and cluster agglomeration. We postulate that at the metastable zone, boundary sufficient water has covered the surface such that solvation can commence, from which then the hydration of the new phase can start.
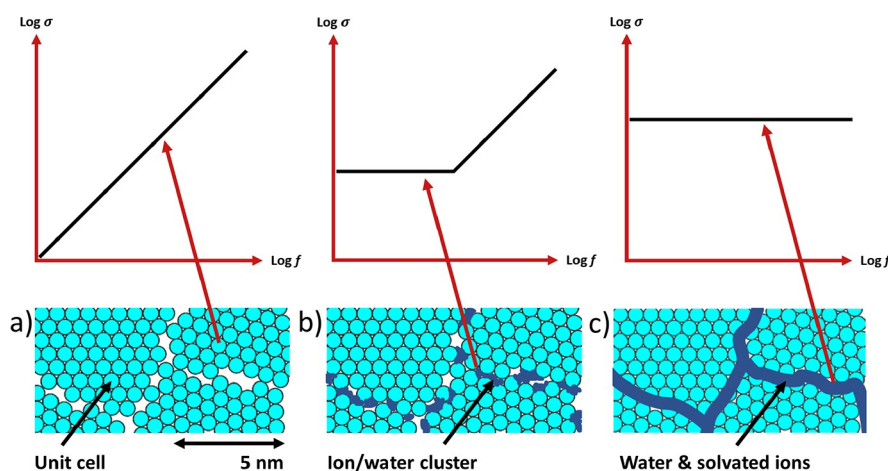
Figure 12. Schematic representation of the different stages of water adsorption on an anhydrous K_2CO_3 crystal surface. In the top, the x axis is the frequency f and the y axis is the conductivity σ. (a) Dry crystal in the absence of water only capacitance is observed. (b) Local adsorbed water with dissolved ions indicated by low frequency conductivity. (c) Whole surface is covered and long-range mobility is observed.

A schematic interpretation of all stages of water adsorption, cluster formation, and cluster agglomeration is shown in Figure 12.

On the left, the anhydrate (Figure 12a) in the absence of adsorbed water is shown. Here, only induced polarization of the bulk crystal can occur and there is no ionic mobility. In Figure 12b, in the MSZ, the initial stages of water adsorption and water/ion cluster formation are shown. These initial clusters will form at locations where the free energy for cluster formation is the lowest. There is a difference in free energy required to solvate ions from smooth faces and from defect-rich crystallite surfaces.[13,29,30] For the anhydrate in the MSZ, solvation can commence at defects, but an induction period is required for nuclei of the hydrate to stabilize and grow. Moreover, Dai et al.[31] reported that adsorbed water on a NaCl crystal surface probably dissolves and detaches ions at the steps of a crystal surface. This is then linked to differences in local water concentration, ionic solvation, and mobility. At low RH, water is primarily adsorbed on edges where there is a higher surface energy. Subsequently, at medium RH, step diffusion of the solvated ions takes place.

In Figure 12b, when the supersaturation is increased, clusters will grow and start to agglomerate by which conductive behavior starts to dominate at lower frequencies. This corresponds to water vapor pressures in the metastable zone close to equilibrium. In Figure 12c, complete coverage of the crystal surface is reached and conductive behavior dominates over the whole range of frequencies. This corresponds to vapor pressures close to and above the MZS boundary.

Generally, supersaturation (p/p_{eq}) is regarded as a driver for nucleation. In the work of Sögütoglu et al.,[10] supersaturation is not sufficient to overcome the energy barrier for nucleation, i.e., ΔG in eq 2. This paper shows that also mobility is limited in the MSZ and a significant increase in mobility has been observed above the MSZ. This indicates that the kinetic prefactor κ (eq 3) is also a function of the supersaturation. Moreover, since mobility is strongly correlated to the solvation of ions from the surface, we postulate that the energy required for the solvation of the bulk crystal phase is a barrier for nucleation. Therefore, to facilitate the hydration reaction, mobility has to be introduced by the solvation of ions from the surface and the interfacial energy has to be overcome, causing a barrier in free energy.

6. CONCLUSIONS

This work aimed to get a more detailed understanding on the hydration mechanism and determine the link between surface mobility and metastability. To that extent, ionic mobility is probed and linked to the hydration mechanism using electrochemical impedance spectroscopy (EIS). It has been shown that mobility is a prerequisite for nucleation and that the mechanism of cluster formation probably occurs via the attachment of ions. Therefore, sufficient mobility must be introduced for the diffusion of ions and water. It has been shown that the metastable zone is both a consequence of the energy barrier for nucleation and the low ion mobility at low vapor pressures.

Moreover, it has been shown that the MSZ boundary in pure water vapor conditions matches nicely with the atmospheric case.[10] The mobility of ions on the surface of K_2CO_3 has been investigated under pure water vapor conditions as a function of supersaturation. Probing mobility at rapidly changing water conditions indicated that the measured ionic mobility could probably be attributed to mobile water and ions at crystal surfaces. This work shows that there is surface mobility already in the MSZ and that this mobility increases with increasing water vapor pressure. At the metastable zone boundary, a significant increase in ionic mobility is observed, facilitated by water adsorption.

Analyzing mobility in greater detail as a function of frequency showed that the initial water adsorption (at low supersaturation) is localized in clusters; at increasing supersaturation, these clusters agglomerate into larger islands; and the ionic mobility increases. Subsequently, the whole surface of the crystallites is covered, which was observed by long-range transport of ions (conductivity). For future work, it would be most interesting to determine the surface area of the samples to derive detailed information about the amount of water and film thickness.

This work can be of significant importance in view of heat storage application since a better understanding of the limiting mechanism in the metastable zone gives us handles to manipulate its behavior, e.g., introducing more mobility to reduce the metastable zone width and thereby increasing the temperature output window. Moreover, introducing more mobility can also be a way to enhance material kinetics.

■ AUTHOR INFORMATION

Corresponding Author

Henk Huinink − *Eindhoven University of Technology, 5600 MB, Eindhoven, The Netherlands; EIRES, 5612 AX, Eindhoven, The Netherlands;* ⓘ orcid.org/0000-0003-2417-0576; Email: h.p.huinink@tue.nl

Authors

Jelle Houben − *Eindhoven University of Technology, 5600 MB, Eindhoven, The Netherlands*

Dennis Langelaan − *Eindhoven University of Technology, 5600 MB, Eindhoven, The Netherlands*

Luc Brinkman − *Eindhoven University of Technology, 5600 MB, Eindhoven, The Netherlands*

Hartmut R. Fischer − *TNO Materials Solutions, 5656 AE, Eindhoven, The Netherlands;* ⓘ orcid.org/0000-0001-9724-4922

Olaf C.G. Adan − *Eindhoven University of Technology, 5600 MB, Eindhoven, The Netherlands; TNO Materials Solutions, 5656 AE, Eindhoven, The Netherlands*

Complete contact information is available at:
https://pubs.acs.org/10.1021/acs.cgd.2c00416

Notes

The authors declare no competing financial interest.

■ REFERENCES

(1) Xu, J.; Wang, R. Z.; Li, Y. A review of available technologies for seasonal thermal energy storage. *Sol. Energy* **2014**, *103*, 610−638.

(2) Veselovskaya, J. V.; Derevschikov, V. S.; Kardash, T. Y.; Stonkus, O. A.; Trubitsina, T. A.; Okunev, A. G. Direct CO2 capture from ambient air using K_2CO_3/Al_2O_3 composite sorbent. *Int. J. Greenhouse Gas Control* **2013**, *17*, 332−340.

(3) Clark, R. J.; Mehrabadi, A.; Farid, M. State of the art on salt hydrate thermochemical energy storage systems for use in building applications. *J. Energy Storage* **2020**, *27*, No. 101145.

(4) Yan, T.; Li, T. X.; Wang, R. Z. *Thermochemical heat storage for solar heating and cooling systems, in: Advances in Solar Heating and Cooling*; Elsevier Inc, 2016 pp. 491−522.

(5) N'tsoukpoe, K. E.; Liu, H.; Le Pierrès, N.; Luo, L. A review on long-term sorption solar energy storage. *Renewable Sustainable Energy Rev.* **2009**, *13*, 2385−2396.

(6) Tatsidjodoung, P.; Le Pierrès, N.; Luo, L. A review of potential materials for thermal energy storage in building applications. *Renewable Sustainable Energy Rev.* **2013**, *18*, 327−349.

(7) Fopah Lele, A.; Kuznik, F.; Rammelberg, H. U.; Schmidt, T.; Ruck, W. K. Thermal decomposition kinetic of salt hydrates for heat storage systems. *Appl. Energy* **2015**, *154*, 447−458.

(8) Kousksou, T.; Bruel, P.; Jamil, A.; El Rhafiki, T.; Zeraouli, Y. Energy storage: Applications and challenges. *Sol. Energy Mater. Sol. Cells* **2014**, *120*, 59−80.

(9) Donkers, P. A.; Sögütoglu, L. C.; Huinink, H. P.; Fischer, H. R.; Adan, O. C. A review of salt hydrates for seasonal heat storage in domestic applications. *Appl. Energy* **2017**, *199*, 45−68.

(10) Sögütoglu, L. C.; Steiger, M.; Houben, J.; Biemans, D.; Fischer, H. R.; Donkers, P.; Huinink, H.; Adan, O. C. Understanding the Hydration Process of Salts: The Impact of a Nucleation Barrier. *Cryst. Growth Des.* **2019**, *19*, 2279−2288.

(11) Maier, S.; Salmeron, M. How Does Water Wet a Surface? *Acc. Chem. Res.* **2015**, *48*, 2783−2790.

(12) Wise, M. E.; Buseck, P. R.; Martin, S. T.; Russell, L. M. Water uptake by nacl particles prior to deliquescence and the phase rule. *Aerosol Sci. Technol.* **2008**, *42*, 281−294.

(13) Peters, S. J.; Ewing, G. E. Water on salt: An infrared study of adsorbed H_2O on NaCl(100) under ambient conditions. *J. Phys. Chem. B* **1997**, *101*, 10880−10886.

(14) Prakash, S.; Yeom, J. *Nanofluidics and Microfluidics: Systems and Applications*; Elsevier Inc., 2014.

(15) Peters, S. J.; Ewing, G. E. Thin Film Water on NaCl(100) under Ambient Conditions: An Infrared Study. *Langmuir* **1997**, *13*, 6345−6348.

(16) Peters, J.; Ewing, G. E. Water on salt: An infrared study of adsorbed H_2O on NaCl(100) under ambient conditions. *J. Phys. Chem. B* **1997**, *101*, 10880−10886.

(17) Derjaguin, B. V.; Churaev, N. V. Structure of water in thin layers. *Prog. Surf. Sci.* **1992**, *40*, 422−428.

(18) Limousin, G.; Gaudet, J. P.; Charlet, L.; Szenknect, S.; Barthes, V.; Krimissa, M. Sorption isotherms: A review on physical bases, modeling and measurement. *Appl. Geochem.* **2007**, *22*, 249−275.

(19) Mullin, J. W.; Osman, M. M. The nucleation and precipitation of nickel ammonium sulphate crystals from aqueous solution. *Krist. Tech.* **1973**, *8*, 471−481.

(20) Kalikmanov, V. I. Classical nucleation theory. In *Nucleation theory*; Springer: Dordrecht, 2013, 17−41.

(21) Houben, J.; Sögütoglu, L.; Donkers, P.; Huinink, H.; Adan, O. K_2CO_3 in closed heat storage systems. *Renewable Energy* **2020**, *166*, 35−44.

(22) Nielsen, A. E.; Söhnel, O. Interfacial tensions electrolyte crystal-aqueous solution, from nucleation data. *J. Cryst. Growth* **1971**, *11*, 233−242.

(23) Machlin, E. S. *An Introduction to Aspects of Thermodynamics and Kinetics Relevant to Materials Science*, September, 2007.

(24) Gilman, J. J. *Direct Measurements of the Surface Energies of Crystals 2208* (2004).

(25) Lipsett, S. G.; Johnson, F. M. G.; Maass, O. The Surface Eenergy and the Heat of Solution of Solid Sodium Chloride. I. *J. Am. Chem. Soc.* **2002**, *49*, 925−943.

(26) Kinloch, A. *Adhesion and Adhesives*, 1st edition ed., Chapman Hall, 1987.

(27) D. C. Corporation. Level Measurement of Liquids, 1997, https://www.deltacnt.com/resources/level-and-flow/99-00032/.

(28) Xu, L.; Bluhm, H.; Salmeron, M. An AFM study of the tribological properties of NaCl (100) surfaces under moist air. *Surf. Sci.* **1998**, *407*, 251−255.

(29) Foster, M. C.; Ewing, G. E.; Foster, M. C.; Ewing, G. E. Adsorption of water on the NaCl (001) surface. II. An infrared study at ambient temperatures. *J. Chem. Phys.* **2000**, *112*, 6817−6826.

(30) Cantrell, W.; McCrory, C.; Ewing, G. E. Nucleated deliquescence of salt. *J. Chem. Phys.* **2002**, *116*, 2116−2120.

(31) Dai, Q.; Hu, J.; Salmeron, M. Adsorption of Water on NaCl (100) Surfaces: Role of Atomic Steps. *J. Phys. Chem. B* **1997**, *101*, 1994−1998.